

Optical appearance of the Konoplya-Zhidenko rotating non-Kerr black hole surrounded by a thin accretion disk

Ke-Jian He,^{1,*} Chen-Yu Yang,^{1,†} and Xiao-Xiong Zeng^{2,1,‡}

¹*Department of Mechanics, Chongqing Jiaotong University,
Chongqing 400000, People's Republic of China*

²*College of Physics and Electronic Engineering,
Chongqing Normal University, Chongqing 401331, People's Republic of China*

In this study, we analyze the observational images of a Konoplya-Zhidenko rotating non-Kerr black hole, wherein a thin accretion disk, serving as the sole background light source, is situated on the equatorial plane of the black hole. The inner boundary of the thin accretion disk extends to the event horizon, and the accretion material in the disk exhibits two different motion behaviors, that is, it moves along the critical plunging orbit inside the innermost stable circular orbit (ISCO) and follows the Keplerian orbit outside the ISCO. The shadow image is captured on the imaging plane of a zero angular momentum observer utilizing advanced fisheye camera ray-tracing techniques. The results demonstrate that an image consistently reveals a dark region encircled by a narrow photon ring, which is called the inner shadow. At low observation inclination angles, the observation intensity is highly concentrated, with the lensed image of accretion disk being superimposed on the direct image. As observation inclination angle increases, the direct and lensed images gradually separate, becoming distinctly distinguishable and forming a hat-like structure. Furthermore, variations in the parameter space and observation angle will influence pertinent image characteristics, including image symmetry, the range or deformation degree of the inner shadow. We further examined the distinctive characteristics of images observed in both prograde and retrograde accretion disk scenarios. Subsequently, we also examined the redshift distribution on the disk. The findings indicate that while variations in relevant parameters do influence the redshift distribution, the primary factor is the change in observational inclination. The observer can detect both redshift and blueshift phenomena on the screen when viewed at a higher observation angle.

*Electronic address: kjhe94@163.com

†Electronic address: chenyuyang2024@163.com

‡Corresponding author: xxzengphysics@163.com

I. INTRODUCTION

In accordance with the theory of general relativity (GR), extremely dense celestial bodies, including black holes, are known to exist within our universe, and the quest to identify these entities has become a focal point of research in astronomy and astrophysics. Notwithstanding a plethora of groundbreaking advancements in the study of black holes, the paramount obstacle persists in the paucity of observation data. As posited by the GR, there are two primary methods for acquiring information about black holes: observing gravitational lensing effect and detecting gravitational waves. In 2016, the detection of the GW150914 gravitational wave event by the LIGO-Virgo collaboration, resulting from the merger of two black holes with masses 29 and 36 times that of the sun, respectively, furnished robust empirical support for the existence of these enigmatic entities[1–3]. Very recently, the Event Horizon Telescope (EHT) has played a pivotal role in capturing images of the supermassive black hole at the center of the galaxy Messier 87 (M87*), utilizing 1.3 mm interferometric observations[4–9]. Subsequently, the EHT unveiled an image of Sagittarius A* (Sgr A*), which not only confirmed the presence of a supermassive black hole at the center of the Milky Way galaxy but also validated the analysis of stellar trajectories [10–15]. These seminal observations not only reinforce the theoretical underpinnings of GR but also furnish invaluable data for investigating the physical characteristics of black holes and the nature of extreme cosmic environments, ushering in a new epoch in black hole physics research.

In the images of the EHT, it is evident that there is a bright circular structure, which is interpreted as the photon ring, and a central dark region, referred to as the black hole shadow. A black hole shadow is formed as a result of a strong gravitational lensing effect and is defined as the collection of directions in the observer’s sky from which no signal from the source can reach the observer[16]. The intrinsic properties of black hole shadow are precisely defined by the fundamental photon orbits and the spacetime structure surrounding the black hole. According to the EHT report, it is clearly shown that the angular size of the photon ring of Sgr A* is consistent with the radius of the shadow critical curve derived from GR, within a margin of 10%[10–15]. Actually, the shadow cast by the Schwarzschild black hole was initially discussed by Synge [17], and the formula for calculating the angular radius of the shadow is provided. In [18], Bardeen investigated the shadows produced by Kerr black holes, demonstrating that the shadows of rotating black holes deviate from perfect circularity[19]. Later on, the shadow of a Kerr black hole or a Kerr naked singularity, as discussed by Hioki and Maeda, has been examined through the construction of two observables[20]. The black hole shadow has emerged as a focal point of interest among researchers

and has been extensively studied within various contexts of black hole physics, including regular black holes [21–26], non-commutative black holes [27, 28], black holes surrounded by plasma [29–31], and black holes in modified GR [32–43]. In addition, some important results have been obtained on black hole shadows and photon rings using wave optics in the holographic framework [44–46]. Simultaneously, the investigation into black hole shadows has also advanced research into other facets of black holes, including quasinormal modes and parameter constraints [47–55].

On the other hand, the luminous structures observed in the image are generated by the light emanating from materials within the accretion disk surrounding the black hole. In the actual astronomical environment, a supermassive black hole is typically surrounded by a substantial amount of high-temperature, high-density radiative plasma, forming a luminous accretion disk structure. Thermally synchronized electrons act as the paramount luminous source in the intricate process of black hole imaging. Furthermore, the EHT’s detailed observations of the intricate magnetic field structure surrounding the accretion disk revealed that the magnetic field constrained accretion disk is in precise agreement with the predictions derived from general relativistic magnetohydrodynamic simulation models. Consequently, the characteristics of the luminous regions are intricately associated with the emission properties of the accretion disk, which are influenced by both the specific accretion disk model and the underlying physical mechanisms. In 1979, Lunin considered a model of a thin accretion disk, utilized semi-analytical techniques to simulate the image of a Schwarzschild black hole, and demonstrated that the appearance of the black hole’s shadow is contingent upon the characteristics of the accretion flow and the outer edge of central brightness depression [56]. Considering a relatively simple accretion model, spherical accretion model, some meaningful results are also obtained [57–59]. In the work of [60], Gralla et al. examine Schwarzschild black holes surrounded by a geometrically and optically thin accretion disk, revealing that the bright ring outside the black hole’s shadow consists of direct emissions, a lensing ring, and a photon ring. Subsequently, the model proposed by Gralla et al. was extended to encompass additional scenarios involving matter fields and modified gravity; however, these investigations were confined to the context of spherically symmetric black holes [61–71]. Given the strong magnetic field surrounding the black hole, the thin accretion disk model is extended to the case of a rotating Kerr-Melvin black hole, which is composed of plasma fluids and behaves differently in different regions [72]. This research investigates the utilization of internal shadows and critical curves of a black hole to estimate the magnetic field surrounding it. By considering the thin disk model presented in the work [72], several intriguing studies have also been conducted on alternative models of black holes within modified gravitational backgrounds [73–76].

It is well known that GR exhibits robust completeness in describing gravitational systems, but there is a lack of direct evidence to conclusively confirm that the observed black hole candidates are indeed Kerr black holes. Current observational data do not exclude the possibility that the geometry of these candidates may significantly diverge from the Kerr metric, thereby maintaining an open window for testing alternative gravitational theories. The spacetimes that deviate from the Kerr metric due to rotation are typically referred to as rotating non-Kerr spacetimes, which have been extensively studied in astrophysics. To test the no-hair theorem, Johannsen and Psaltis propose a spacetime solution for a non-Kerr black hole that incorporates not only the mass M and the rotation parameter a , but also introduces an additional deformation parameter to quantify deviations from the Kerr spacetime[77]. This spacetime solution exhibits the same asymptotic behavior as Kerr spacetime in the far-field region, yet it possesses markedly distinct characteristics in the vicinity of the event horizon. Furthermore, the rotation parameter a of the Johannsen-Psaltis non-Kerr spacetime is not constrained by any upper limit, allowing it to describe superrotating black holes $a > M$, a phenomenon that does not occur within the framework of GR. By incorporating a static deformation, Konoplya and Zhidenko introduced a rotating non-Kerr black hole metric that extends beyond the framework of GR[78], representing an axially symmetric vacuum solution to an unspecified alternative theory of gravity[79]. By employing this rotating non-Kerr metric, they discovered that certain non-negligible deviations from Kerr spacetime can also generate the same frequencies of black hole resonance[78]. Furthermore, the constraints imposed by quasi-periodic oscillations and iron line profiles[80–86] lend additional support to the hypothesis that actual astrophysical black holes can be accurately characterized using the Konoplya-Zhidenko rotating non-Kerr metric. Several intriguing studies have explored the properties and characteristics of the Konoplya-Zhidenko rotating non-Kerr black hole spacetime, encompassing aspects such as energy extraction, strong gravitational lensing effects, and magnetic reconnection, among others[87–92].

The shadow is an inherent characteristic of black hole spacetime, it also serves as an experimental platform for testing general relativity and alternative gravitational theories in the context of strong gravitational fields. Consequently, it is anticipated that novel black hole shadow phenomena will emerge in the Konoplya-Zhidenko rotating non-Kerr black hole spacetime as a result of the unique spatial structure characteristics stemming from the deformation parameters. In [93], Wang et al. investigated the shadow cast by the Konoplya-Zhidenko rotating non-Kerr black hole, the results show that the black hole shadow exhibited a spiky feature with minor eyelash-like structures in the case of $a > M$. However, as the deformation parameter increased, the spiky characteristic of the shadow progressively diminished. Then, the shadows of the Konoplya-Zhidenko naked singularity

were also investigated, where the spherical source is considered as the only background source[100]. The findings indicate that these naked singularities can generate both arc and ring shadows during rotation. In this paper, we aim to further investigate the shadows of Konoplya-Zhidenko rotating non-Kerr black holes, with a focus on the thin accretion disk surrounding the black hole as the sole background light source. In this scenario, we will examine the impact of variations in parameter space and observational angle on the observable features of the black hole shadow.

The paper will be completed in the following manner. In Section 2, we will provide a concise introduction to the Konoplya-Zhidenko rotating non-Kerr black hole. In Section 3, we study the shadow of the black hole, and analyzed the deviation from the circularity and the size of shadow. Also, the shadow angular diameter is obtained, and compared with that of M87* and SgrA*. In Section 4, we examine an optically and geometrically thin accretion disk situated on the equatorial plane of the black hole to derive its visually observed appearance. In Section 5, we meticulously scrutinize the impacts of parameters on the redshift factor and the appearance of the inner shadow. Finally, in Section 6, we give a brief conclusion and discussion.

II. THE KONOPLYA-ZHIDENKO ROTATING NON-KERR BLACK HOLE

As a starting point, we will present a succinct overview of the Konoplya-Zhidenko rotating non-Kerr spacetime, which serves as the foundational framework for our comprehensive investigation. The metric presented here, which deviates from the Kerr metric, is a non-Kerr metric that typically arises from deforming the Kerr metric. In the Boyer-Lindquist coordinates, the metric of a rotating non-Kerr black hole in the Konoplya-Zhidenko model can be expressed as[78]

$$ds^2 = -\frac{\mathcal{A}^2(r, \theta) - \mathcal{B}^2(r, \theta) \sin^2 \theta}{\mathcal{C}^2(r, \theta)} dt^2 - 2\mathcal{B}(r, \theta)r \sin^2 \theta dt d\theta + \mathcal{C}^2(r, \theta)r^2 \sin^2 \theta d\varphi^2 + \Sigma(r, \theta)r^2 d\theta^2 + \frac{\Sigma(r, \theta)\mathcal{D}^2(r, \theta)}{\mathcal{A}^2(r, \theta)} \quad (1)$$

in which

$$\begin{aligned} \mathcal{A}^2(r, \theta) &= \frac{r^2 + a^2 - 2Mr}{r^2} - \frac{\xi}{r^3}, & \mathcal{B}(r, \theta) &= \frac{2Ma}{r^2 + a^2 \cos^2 \theta} + \frac{a\xi}{r^2(r^2 + a^2 \cos^2 \theta)}, \\ \mathcal{C}^2(r, \theta) &= \frac{(r^2 + a^2)^2 - a^2 \sin^2 \theta (a^2 + r^2 - 2Mr)}{r^2(r^2 + a^2 \cos^2 \theta)} + \frac{a^2 \xi \sin^2 \theta}{r^3(r^2 + a^2 \cos^2 \theta)}, \\ \mathcal{D}(r, \theta) &= 1, & \Sigma(r, \theta) &= \frac{a^2 \cos^2 \theta + r^2}{r^2}. \end{aligned} \quad (2)$$

In this spacetime, the mass of the black hole is denoted by M , while the rotation parameter is represented by a . Additionally, the deviation from Kerr spacetime is quantified by the deformation

parameter ξ , which degenerates to the general Kerr black hole metric at $\xi = 0$. It is worth mentioning that the presence of the parameter ξ does not significantly alter the asymptotic structure of spacetime at infinity. In other words, in the weak field case at infinity, distinguishing Konoplya-Zhidenko black hole from Kerr black hole becomes challenging. However, the presence of the deformation parameter ξ modifies the behavior of spacetime in close proximity to the event horizon, thereby facilitating tests in the strong field region for potential detection of deviations from the Kerr metric. It is demonstrated that a non-negligible deformations of the Kerr spacetime can lead to the same frequency of black hole resonance, as evidenced by data from GW150914[101]. The event horizon r_h of Konoplya-Zhidenko rotating non-Kerr black hole are determined by

$$\Delta_r = r^2 - 2Mr + a - \frac{\xi}{r} = 0. \quad (3)$$

Obviously, the location of the event horizon is evidently distinct from that of the Kerr black hole, and it explicitly relies on the value of the deformation parameter ξ . The impact of varying the deformation parameter ξ on the event horizon and infinite redshift surface of the Konoplya-Zhidenko rotating non-Kerr black hole can be found in [87]. For the value of the deformation parameter ξ , it can be classified as

$$\begin{cases} \xi \geq \xi_{c1} \equiv -\frac{2}{27}(\sqrt{4M^2 - 3a^2} + 2M)^2(\sqrt{4M^2 - 3a^2} - M), & a < M \\ \xi > 0, & a > M \end{cases} \quad (4)$$

which allows for the existence of event horizon in this specific black hole spacetime, and further details can be found in Refs.[93, 100]. The absence of a horizon occurs when ξ and a lie in other regions, resulting in the emergence of a naked singularity within the spacetime. In light of the Weak Cosmic Censorship Conjecture (WCCC), our exclusive focus will be on scenarios where the existence of the event horizon is ensured, and the values of the relevant parameters adhere to this principle. The value of the deformation parameter ξ determines the quantity and location of the horizon, and these spacetime properties have an impact on the propagation of particles, thereby naturally inducing variations in the shadow cast by the Konoplya-Zhidenko rotating non-Kerr black hole. The Hamiltonian of particles propagation along null geodesics in this spacetime is given by

$$\mathcal{H} = \frac{1}{2}g^{\mu\nu}p_\mu p_\nu = -\frac{u^2}{2}. \quad (5)$$

Where \mathcal{H} represents the Hamiltonian, p_μ denotes the four-momentum of the particle, and u signifies the mass of particles moving in the black hole spacetime, with $u = 0$ indicating null geodesics. By combining the spacetime metric (1) with the Hamiltonian (5), one can find that Hamiltonian \mathcal{H}

being independent of t and φ gives rise to two Killing vectors fields, ∂_t and ∂_φ , which represent the translational and rotational invariance of time. Consequently, this leads to the existence of two conserved quantities for photon motion in the Konoplya-Zhidenko rotating black hole spacetime, which is

$$E = -p_t = -g_{\varphi t}\dot{\varphi} - g_{tt}\dot{t}, \quad L = p_\varphi = -g_{\varphi\varphi}\dot{\varphi} + g_{\varphi t}\dot{t}. \quad (6)$$

In the above equations, the symbol \cdot denotes derivative with respect to the affine parameter λ , while E and L represent the energy and angular momentum along the axis of symmetry. With the aid of these two conserved quantities, the null geodesics of a photon in this particular spacetime can be formulated as a set of four first-order differential equations, that is

$$\dot{t} = E + \frac{(a^2E - aL + r^2E)(2Mr^2 + \xi)}{r^3\Sigma(r, \theta)\mathcal{A}^2(r, \theta)}, \quad (7)$$

$$\dot{\varphi} = \frac{aE \sin^2 \theta (2Mr^2 + \xi) + aLr \cos^2 \theta - L(2Mr^2 - r^3 + \xi)}{r^3\Sigma(r, \theta)\mathcal{A}^2(r, \theta) \sin^2 \theta}, \quad (8)$$

$$\Sigma^2(r, \theta)r^2\dot{r}^2 = \mathbf{R}(r) = -\mathcal{A}^2(r, \theta)(Q_\kappa + (aE - L)^2) + (aL - (a^2 + r^2)E)^2, \quad (9)$$

$$\Sigma^2(r, \theta)r^4\dot{\theta}^2 = \Theta(\theta) = Q_\kappa + a^2E^2 \cos^2 \theta - \frac{\cos^2 \theta L^2}{\sin^2 \theta}. \quad (10)$$

where the quantity Q_κ represents the third conserved constant of photon motion in this particular spacetime, analogous to the Carter constant associated with the Kerr spacetime[93]. The behavior of photons in close proximity to a black hole can be accurately described by equations (7)-(10), thus subsequent discussions on black hole shadows heavily rely on these four differential equations.

III. SHADOW OF THE KONOPLYA-ZHIDENKO ROTATING NON-KERR BLACK HOLE

The shadow shape of the Konoplya-Zhidenko rotating non-Kerr black hole has been investigated to a certain extent under various parameter values[93]. To offer a thorough background, we will provide a concise overview of the procedure involved in acquiring the black hole shadow. It is well known that the shadow boundary of a black hole is uniquely determined by its photon sphere, which always satisfies the conditions $\dot{r} = 0$ and $\ddot{r} = 0$, indicating that

$$\mathbf{R}(r) = -r^2\mathcal{A}^2(r, \theta)(Q_\kappa + (aE - L)^2) + (aL - (a^2 + r^2)E)^2 = 0, \quad (11)$$

and

$$\mathbf{R}'(r) = -4Er(aL - (a^2 + r^2)E) - (Q_\kappa + (aE - L)^2)(2r - 2M + \xi r^{-2}) = 0. \quad (12)$$

In addition, the unstable photon orbit also needs to meet the condition

$$\mathbf{R}''(r) = 8E^2r^2 - 4E(aL - (a^2 + r^2)E) - 2(Q_\kappa + (aE - L)^2)(1 - \xi r^{-3}) = 0. \quad (13)$$

By defining the two impact parameters $\varrho = \frac{L}{E}$ and $\sigma = \frac{Q_\kappa}{E^2}$, one can obtain that

$$\varrho = \frac{2a^2Mr^2 - a^2\xi + (2\mathcal{A}^2(r, \theta)r^3 - 2Mr^2 - 3\xi)r^2}{a(2Mr^2 - \xi - 2r^3)}. \quad (14)$$

and

$$\sigma = -\frac{r^4((6Mr^2 - 2r^3 + 5\xi)^2 - 8a^2(2Mr^3 + 3\xi r))}{a^2(2r^3 - 2Mr^2 + \xi)^2}. \quad (15)$$

The condition for the photon region can be determined, provided that Θ in equation (10) is non-negative, which is

$$\sigma + a^2 \cos^2 \theta \geq \varrho^2 \cot^2 \theta. \quad (16)$$

The motion of photons within the photon sphere can be characterized by ϱ and σ , whereby these two conserved quantities naturally determine the boundary of the black hole shadow. To effectively describe the size and distortion of a black hole shadow, we define two observable physical quantities as described by [94], namely the size of the shadow and the deviation from circularity

$$R_d = \frac{(x_t - x_r)^2 + y_t^2}{2|x_t - x_r|}, \quad \delta_d = \frac{|x_{l'} - x_l|}{R_d}. \quad (17)$$

The top, bottom, and rightmost points of the black hole shadow uniquely determine a reference circle, whose radius is denoted as R_d , approximating the size of the shadow. The parameter δ_d represents the absolute horizontal difference between the leftmost points of the black hole shadow and the reference circle, indicating the degree of deviation from circularity. Specifically, the five reference points (x_t, y_t) , (x_b, y_b) , $(x_r, 0)$, $(x_l, 0)$, and $(x_{l'}, 0)$ correspond to the top, bottom, rightmost, and leftmost points of the shadow, leftmost point of the reference circle, respectively. When $x_l \neq x_{l'}$, $\delta_d \neq 0$. A larger δ_d indicates a greater deviation of the black hole shadow boundary from a circular shape. In Figure 2, we present the effects of the deformation parameter ξ and the rotation parameter a on R_d and δ_d . The results demonstrate that for both $a < M$ and $a > M$, as ξ increases, R_d increases while δ_d decreases, suggesting that the shadow becomes larger and closer to a circular shape.

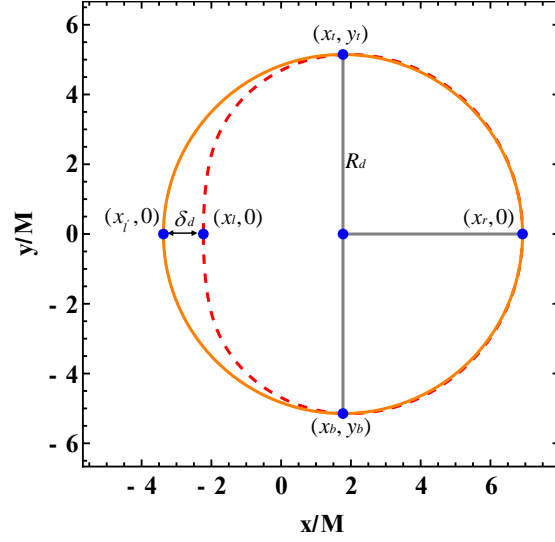


FIG. 1: The black hole shadow and the reference circle. In the figure, the red outline represents the black hole shadow, and the orange outline represents the reference circle. The radius of the reference circle is R_d , and the absolute horizontal difference between the leftmost points of the reference circle and the black hole shadow is δ_d .

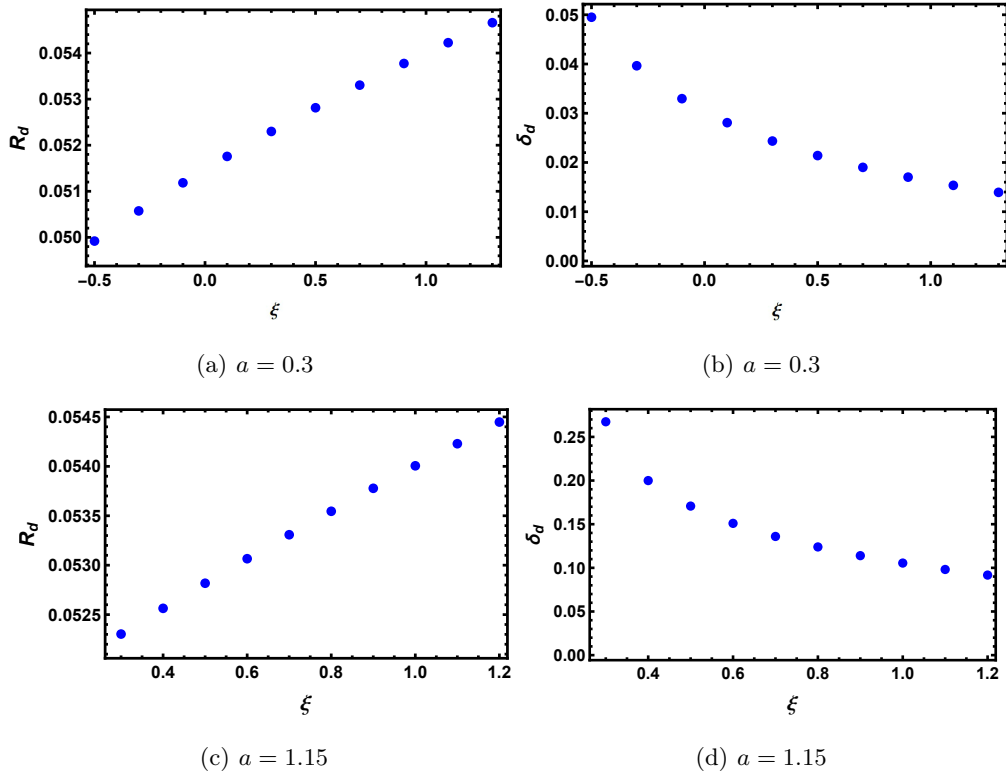


FIG. 2: The observable R_d and δ_d for $r_o = 100$, $\theta_o = \pi/2$ and $M = 1$.

On the other hand, as described by [95–97], the angular diameter $\mathcal{D} = 2\tilde{R}_d \frac{\mathcal{M}}{D_o}$ is used in astronomical observations to describe the size of the black hole shadow. Here, D_o denotes the distance between the black hole and the observer, \tilde{R}_d is the shadow radius when the screen is placed at the black hole’s location, which is related to the shadow size R_d and can be calculated using a simple geometric relation, and \mathcal{M} is the mass of the black hole. When the black hole is far from the observer, the angular diameter can be quantitatively expressed as

$$\mathcal{D} = 2 \times 9.87098 \tilde{R}_d \left(\frac{\mathcal{M}}{M_\odot} \right) \left(\frac{1 \text{kpc}}{D_o} \right) \mu\text{as}. \quad (18)$$

Using the above equation, we calculate the theoretical angular diameters of Sgr A* and M87* under different parameters by assuming that their background spacetime is given by equation (1), and compare the results with astronomical observations. For M87*, its distance from Earth is $D_o = 16.8$ kpc, and its estimated black hole mass is $\mathcal{M} = (6.5 \pm 0.7) \times 10^6 M_\odot$, while the observed shadow diameter is $\mathcal{D}_{\text{M87}^*} = (37.8 \pm 2.7) \mu\text{as}$ [98]. For Sgr A*, its distance from Earth is $D_o = 8$ kpc, and its estimated black hole mass is $\mathcal{M} = (4.0_{-0.6}^{+1.1}) \times 10^6 M_\odot$, while the observed shadow diameter is $\mathcal{D}_{\text{SgrA}^*} = (48.7 \pm 7) \mu\text{as}$ [99].

In Figure 3, we present the estimated intervals of the angular diameters \mathcal{D} for Sgr A* and M87*. The first row corresponds to Sgr A*, and the second row corresponds to M87*. In the figure, the red solid lines represent the 1σ confidence interval of \mathcal{D} , the blue solid lines represent the 2σ confidence interval, and the orange line segments indicate the estimated intervals, with their endpoints highlighted by thick black ticks. When $M > a = 0.5$, for $-0.5 \leq \xi \leq 2.5$, the estimated intervals of the angular diameters for both Sgr A* and M87* increase with ξ . Similarly, when $M < a = 1.15$, the estimated intervals of the angular diameters for both objects also increase with ξ . All the estimated intervals are within the 1σ confidence interval, indicating that whether $a < M$ or $a > M$, the astronomical observations impose weak constraints on the deformation parameter ξ for both M87* and Sgr A*.

The acquisition of the corresponding geodesic equation alone is insufficient; it is imperative to also designate a suitable observer within spacetime. As a general selection, we consider an observer with zero axial angular momentum, also known as a zero angular momentum observer (ZAMO). When the position of ZAMO is denoted as $(t_O, r_O, \theta_O, \varphi_O)$ in the spacetime, a locally orthonormal frame can be established within the vicinity of the observer, which is

$$\tilde{e}_0 = \tilde{e}_{(t)} = \left(\sqrt{\frac{-g_{\varphi\varphi}}{g_{tt}g_{\varphi\varphi} - g_{t\varphi}^2}}, 0, 0, -\frac{g_{t\varphi}}{g_{\varphi\varphi}} \sqrt{\frac{-g_{\varphi\varphi}}{g_{tt}g_{\varphi\varphi} - g_{t\varphi}^2}} \right), \quad (19)$$

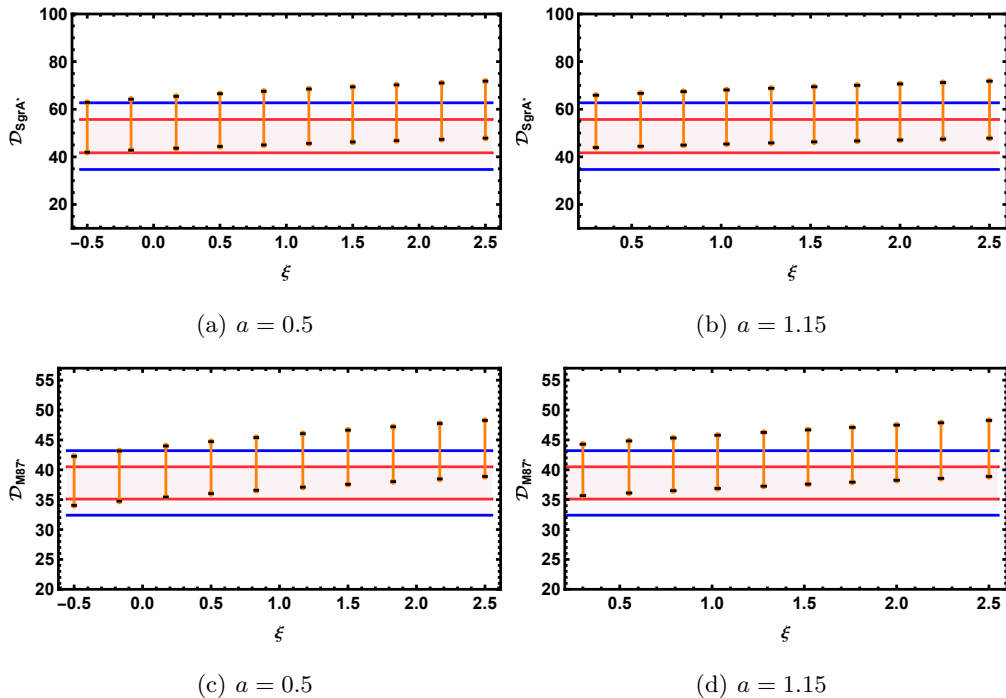


FIG. 3: Estimated intervals of the angular diameter \mathcal{D} . The first row corresponds to Sgr A*, and the second row corresponds to M87*. In the figure, the red and blue solid lines denote the 1σ and 2σ confidence intervals of \mathcal{D} , respectively, while the orange line segments represent the estimated intervals, with their endpoints highlighted by thick black ticks.

$$\tilde{e}_1 = -\tilde{e}_{(r)} = \left(0, -\frac{1}{\sqrt{g_{rr}}}, 0, 0\right), \quad (20)$$

$$\tilde{e}_2 = \tilde{e}_{(\theta)} = \left(0, 0, \frac{1}{\sqrt{g_{\theta\theta}}}, 0\right), \quad (21)$$

$$\tilde{e}_3 = -\tilde{e}_{(\varphi)} = \left(0, 0, 0, -\frac{1}{\sqrt{g_{\varphi\varphi}}}\right). \quad (22)$$

Here, the timelike vector \tilde{e}_0 is considered as the observer's four-velocity, the vector \tilde{e}_1 represents the spatial direction towards the center of the black hole, while $g_{\mu\nu}$ is the component of the background metric at (r_O, θ_O) . It should be emphasized that the above frame is not the only choice, and different frames can be connected through Lorentz transformations. After determining the full light trajectory, the next step is to consider how to image the black hole. One direct approach is to employ a pinhole camera for perspective projection, as described in [93]. This model is straightforward and aligns well with the actual imaging principles; however, it has the limitation of a relatively narrow field of view. Therefore, we will utilize the imaging methodology detailed in [102], commonly known as the fisheye lens camera model. By employing the stereographic projection

technique, the detection of a photon in the image plane corresponds to the optical perspective of an observer, who can be considered analogous to a camera, see Figure 4. The position of observer

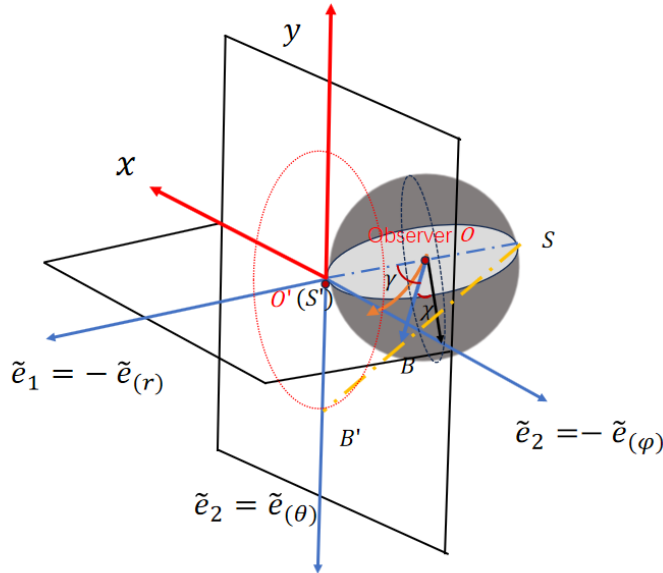


FIG. 4: The ZAMO tetrad and celestial coordinates (γ, χ) based on the method of stereographic projection. The gray sphere situated on the right side of the image symbolizes the three-dimensional subspace from the observer's perspective, whereas the plane (x, y) denotes the imaging plane.

in the coordinate system is represented by the O point in Figure 4, while the orange curve indicates the direction in which the photon traveling along the geodesic arrives at the observer. Moreover, the tangential vector of the photon geodesic at point O is denoted as \overrightarrow{OB} , representing the projection of the tangent vector onto the three-dimensional subspace of the observer. The determination of the apparent position and shape of the black hole shadow in the observer plane, i.e., locating the photon that the observer can receive, necessitates the introduction of a celestial coordinate system (γ, χ) . Specifically, the construction involves creating a three-dimensional sphere centered at O , with OB as the radius. In the equatorial plane, the diameter SS' aligns with \tilde{e}_1 , and subsequently, the angle between OS' and \overrightarrow{OB} determines the first celestial coordinate γ . The central point O' of the imaging plane lies on the line containing the diameter SS' and is perpendicular to the equatorial plane, while $\overrightarrow{O'B'}$ represents the projection of the vector \overrightarrow{OB} onto the imaging plane. The point Q is designated as the intersection between the line connecting points B' and S and the three-dimensional sphere, while another celestial coordinate χ represents the angle formed by OQ and \tilde{e}_2 .

By employing celestial coordinates (γ, χ) , the tangent vectors of null geodesics followed by photons, i.e., $s(\tau) = \{t(\tau), r(\tau), \theta(\tau), \varphi(\tau)\}$, in the observer's frame can be expressed as linear combinations of $(\tilde{e}_0, \tilde{e}_1, \tilde{e}_2, \tilde{e}_3)$, that is

$$\dot{s} = |\overrightarrow{OB}|(-\delta\tilde{e}_0 + \cos\gamma\tilde{e}_1 + \sin\chi\cos\gamma\tilde{e}_2 + \sin\gamma\sin\chi\tilde{e}_3). \quad (23)$$

In the above equation, the negative sign before \tilde{e}_0 is introduced to ensure that the tangent vector points forward, while the symbol \cdot denotes the partial derivative with respect to the affine parameter τ . Since the trajectory of a photon is independent of its energy, for simplicity, one can set the energy of the photon observed by the camera to 1, which is

$$E_C = 1 = |\overrightarrow{OB}| \cdot \delta = -\frac{E}{\sqrt{g_{tt}}} |_{(r_O, \theta_O)}. \quad (24)$$

In the fram of ZAMO, the four-momentum of photons is denoted as $p_{(\mu)} = p_\nu \tilde{e}'_{(\mu)}$, and the term of $p_{(\mu)}$ is derived from equations (7)-(10), while $\tilde{e}'_{(\mu)}$ can be obtained through equations (19)-(22). The relationship between the four-momentum of a photon $p_{(\mu)}$ and celestial coordinates (γ, χ) is established with

$$\cos\gamma = \frac{p^{(1)}}{p^{(0)}}, \quad \tan\chi = \frac{p^{(3)}}{p^{(2)}}. \quad (25)$$

The acquisition of an image of a black hole requires the transformation of celestial coordinates (γ, χ) onto the observation plane. The imaging plane can be equipped with a standard Cartesian coordinate system (x, y) , which establishes a precise correspondence with the celestial coordinates, which is

$$x = -2|\overrightarrow{OB}| \tan \frac{\gamma}{2} \sin \chi, \quad y = -2|\overrightarrow{OB}| \tan \frac{\gamma}{2} \cos \chi. \quad (26)$$

In essence, it determines the initial momentum value of the photon at the ZAMO as well as its initial position. To analyze the shape and size of the black hole shadow seen by equatorial observers under a region of strong gravitational field, one can map the shadow image of a Konoplya-Zhidenko rotating non-Kerr black hole at different ξ and a values. Based on the findings[93], it is evident that the shape and size of the black hole's shadow are contingent upon its corresponding parameter space, and that the shadow shape of the black hole exhibits a cusp silhouette with small eye lashes at specific parameter values.

IV. THIN ACCRETION DISK MODEL AND THE OPTICAL APPEARANCE OF BLACK HOLE

In our universe, black holes are typically encompassed by copious amounts of matter, such as gas and dust, which undergoes accelerated motion due to the immense gravitational force exerted by the black hole. This vigorous movement leads to the emission of high-energy radiation resulting from intense friction and heating processes. As a result, a bright accretion disk exists near the black hole. Considering that the millimeter-wave images of supermassive black holes are predominantly influenced by the presence of their accretion disks, we will employ a specific model that represents the accretion disk as an illuminating source to further investigate the imaging characteristics of a Konoplya-Zhidenko rotating non-Kerr black hole. The aim is to clarify the distinct impact on the observable characteristics of accretion disk structures that arises from modifications to the geometric properties of spacetime within a Konoplya-Zhidenko rotating non-Kerr black hole paradigm.

A. Configuration of the thin accretion disk model

The analysis of the accretion disk can offer valuable insights into the fundamental physical mechanisms governing this intricate system. Therefore, it is necessary to elucidate certain specific aspects of this accretion model: i) the accretion disk model is characterized by its extreme thinness in the geometric and optical, being situated precisely on the equatorial plane; ii) the material comprising the accretion disk consists of electrically neutral free plasma that moves along an equatorial timelike geodesic; iii) the accretion disks exhibit a range of widths, featuring an outer radius surpassing that of the innermost stable circular orbit (ISCO) and an inner radius extending up to the event horizon r_h of the black hole. The ISCO is an important indicator, and its radius can be used along with the radius of the inner boundary of the accretion disk to calculate the energy emission efficiency, which measures how efficiently the rest mass energy of matter is converted into radiative energy. Moreover, the viscosity of the accretion disk induces an outward transfer of angular momentum by the orbiting accretion material around the black hole, resulting in a gradual migration of particles towards the ISCO region in Keplerian motion. The particles undergo acceleration and spiral towards the event horizon until they reach the black hole, and it has been experimentally confirmed that the particle motion mechanism during this process is consistent with astrophysical observations[103]. In recent work [72], the behavior of particle motion in the accretion disk has been well explained. Specifically, the ISCO serves as a demarcation line that segregates particle behavior

within the accretion disk into two distinct categories: the region encompassing ISCO ($r < r_{isco}$), where particles undergo a critical plunging orbits, and the outer region beyond ISCO ($r > r_{isco}$), where particles maintain a stable circular orbit. In the spacetime of (1), the ISCO position of a black hole is given by

$$V_e(r)|_{r=r_{isco}} = 0, \quad \partial_r V_e(r)|_{r=r_{isco}} = 0, \quad \partial_r^2 V_e(r)|_{r=r_{isco}} = 0. \quad (27)$$

The term $V_e(r)$ denotes the effective potential, and a massive neutral particle in the equatorial plane ($\theta = \pi/2$) with four-velocity u^a can be defined as

$$V_e(r, \mathcal{E}, \mathcal{L}) = 1 + g^{tt}\mathcal{E}^2 + g^{t\varphi}\mathcal{L}^2 - 2g^{t\varphi}\mathcal{E}\mathcal{L}. \quad (28)$$

Here, \mathcal{E} and \mathcal{L} are two conserved quantities, denoting the specific energy and specific angular momentum of the massive neutral particle, that is

$$\mathcal{E} = -\frac{g_{tt} + g_{t\varphi}\overline{\mathbf{W}}}{\sqrt{-g_{tt} - 2g_{t\varphi}\overline{\mathbf{W}} - g_{\varphi\varphi}\overline{\mathbf{W}}^2}}, \quad (29)$$

$$\mathcal{L} = -\frac{g_{t\varphi} + g_{\varphi\varphi}\overline{\mathbf{W}}}{\sqrt{-g_{tt} - 2g_{t\varphi}\overline{\mathbf{W}} - g_{\varphi\varphi}\overline{\mathbf{W}}^2}}, \quad (30)$$

and $\overline{\mathbf{W}}$ denotes the angular velocity, which is

$$\overline{\mathbf{W}} = \frac{d\varphi}{dt} = \frac{\partial_r g_{t\varphi} + \sqrt{\partial_r^2 g_{t\varphi} - \partial_r g_{tt} \partial_r g_{\varphi\varphi}}}{\partial_r g_{\varphi\varphi}} \quad (31)$$

In the accretion disk within the range $r_h < r \leq r_{isco}$, the particle falls towards the black hole on a critical plunging orbits, and its four-velocity are

$$u_f^t = -g^{tt}\mathcal{E}_i + g^{t\varphi}\mathcal{L}_i, \quad (32)$$

$$u_f^\varphi = -g^{t\varphi}\mathcal{E}_i + g^{\varphi\varphi}\mathcal{L}_i, \quad (33)$$

$$u_f^\theta = 0, \quad (34)$$

$$u_f^r = -\sqrt{-\frac{1 + g_{tt}u_f^t u_f^t + 2g_{t\varphi}u_f^t u_f^\varphi + g_{\varphi\varphi}u_f^\varphi u_f^\varphi}{g_{rr}}}. \quad (35)$$

In the above equations, \mathcal{E}_i and \mathcal{L}_i are the conserved quantities of the particle at ISCO, and the minus sign before the square root indicates that the direction is toward the black hole. Outside the ISCO $r > r_{isco}$, the four-velocity u_c^μ is governed by

$$u_c^\mu = \sqrt{\frac{1}{-g_{tt} - 2g_{t\varphi}\overline{\mathbf{W}} - g_{\varphi\varphi}\overline{\mathbf{W}}^2}}(1, 0, 0, \overline{\mathbf{W}}). \quad (36)$$

In the process of tracing the light ray path, multiple intersections with the accretion disk in the equatorial plane may occur, resulting in varying radial coordinates at each intersection, see Figure 5. In Figure 5, we illustrate the trajectory of a complete light ray which is depicted by the or-

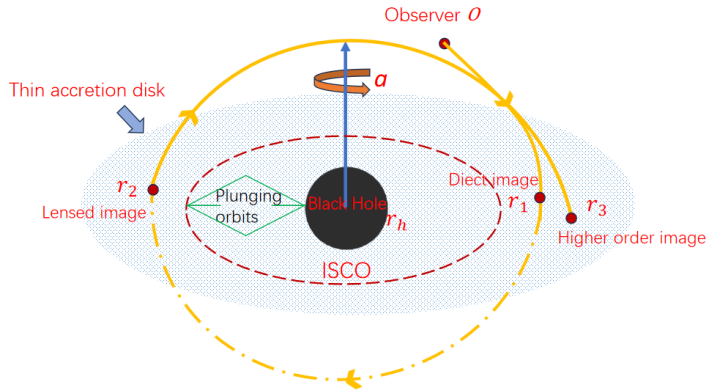


FIG. 5: Imaging the black hole with a thin accretion disks, where the black sphere denotes the black hole, the blue elliptical disk represents the thin accretion disk, and the red dashed line indicates the ISCO. Additionally, the orange curve represents a complete path of light that can be received by the observer.

ange line, where the black sphere represents the black hole and the dotted red line indicates the position of the ISCO. In addition, a thin blue elliptical disk placed on the equatorial surface of the black hole indicates a thin accretion disk. The position of the intersection point is denoted as $r_n(x, y) |_{n=1,2,3\dots N}$, which serves as the definition for the transfer function, and N represents the maximum number of intersection points. In fact, the function $r_n(x, y)$ generates the n^{th} image of the accretion disk, that is, the direct image corresponds to the case of $n = 1$, while the lens image (or higher-order images) produced on the screen corresponds to $n = 2$ (or $n = 3$). Regardless of factors such as the reflection effect and thickness, the intensity of the light received by the observer increases each time a light ray intersects with the accretion disk. In this case, the intensity of the observation on the observation screen can be expressed as

$$\mathcal{I}_o = \sum_{n=1}^N f_n g_n^3 \mathcal{J}_n(r). \quad (37)$$

where f_n is the fudge factor which is fixed to $f_n = 1$. Taking into account that the black hole image captured by the EHT is observed at a wavelength of 1.3 mm (230 GHz), one can select the emissivity of the thin disk to be a second-order polynomial in log-space, which is

$$\mathcal{J}(r) = \exp \left[-\frac{1}{2} \mathcal{Z}^2 - 2\mathcal{Z} \right], \quad \mathcal{Z} = \log \frac{r}{r_h}. \quad (38)$$

In addition, the term g_n^3 represents the redshift factor, which is defined as the ratio of the observed frequency to the emission frequency at radius r_n , that is

$$g_n = \frac{\nu_{obs}}{\nu_n}. \quad (39)$$

Here, the observed frequency by the observer is denoted as ν_{obs} , while the frequency observed by the local static frames co-moving with the emission profiles is represented as ν_n . The factor g_n^3 is applicable to the intensity of a specific frequency, whereas g_n^4 is suitable for integrated intensity[104]. Naturally, the specific forms of the redshift factor differ in the inner and outer regions of the ISCO due to significant disparities in particle emission spectra between these two domains. The accretion flow beyond the ISCO moves along a circular orbits, and its corresponding redshift factor can be expressed as

$$g_n^c = \frac{\eta(1 - v \frac{p_\varphi}{p_t})}{\zeta(1 + \overline{\mathbf{W}} \frac{p_\varphi}{p_t})} \Big|_{r=r_n}, \quad r > r_i, \quad (40)$$

where

$$v = \frac{g_{t\varphi}}{g_{\varphi\varphi}}, \quad \eta = \sqrt{-\frac{g_{\varphi\varphi}}{g_{tt}g_{\varphi\varphi} - g_{t\varphi}^2}}, \quad \zeta = \sqrt{\frac{-1}{g_{tt} + 2g_{t\varphi}\overline{\mathbf{W}} + g_{\varphi\varphi}\overline{\mathbf{W}}^2}}. \quad (41)$$

In addition, the ratio of the observed energy on the screen to the energy along a null geodesic is $e = \frac{p(t)}{p_t}$, that is

$$e = \frac{p(t)}{p_t} = \eta(1 - v \frac{p_\varphi}{p_t}). \quad (42)$$

In the context of asymptotically flat spacetime, when the observer is positioned at an infinite distance, it is permissible to assign a value of e as $e = 1$. In the region within ISCO, the accretion flow is moving along the critical plunge orbit, and its redshift factor is

$$g_n^f = -\frac{1}{u_f^r p_r / p_t - \mathcal{E}_i(g^{tt} - g^{t\varphi} p_\varphi / p_t) + \mathcal{L}_i(g^{\varphi\varphi} p_\varphi / p_t + g^{t\varphi})} \Big|_{r=r_n}, \quad r < r_i. \quad (43)$$

Within the framework of the accretion thin disk model, one can explicitly simulate the visual representation of a Konoplya-Zhidenko rotating non-Kerr black hole on the display by using the redshift factor and the emission model of the disk.

B. Observational appearance of the black hole

The visualization image of the Konoplya-Zhidenko rotating non-Kerr black hole illuminated by the accretion disk can be achieved using the backward ray-tracing technique, which involves tracing

the light path backwards from the observer's position, based on the aforementioned accretion thin disk model. The inner radius of the accretion disk is set to match the event horizon $r_{in} = r_h$, while the outer radius is defined as $r_{out} = 20M$, thus achieving an extension of the accretion disk up to the event horizon. By considering the motion of the accretion disk, one can account for two possibilities: prograde and retrograde, acknowledging the presence of both forward and backward photons in the Konoplya-Zhidenko rotating non-Kerr black hole.

Under thin disk accretion with prograde flows, Figure 6 and Figure 7 illustrates the optical appearance of a Konoplya-Zhidenko rotating non-Kerr black hole with different parameter configurations. The selection of three distinct observation inclination angles includes one angle, $\theta_o = 17^\circ$, which corresponds to the imaging angle for M87* as determined by the EHT. The case depicted in Figure 6 corresponds to situations where the value of the rotation parameter a exceeds that of the mass M ($a < M$), whereas Figure 7 represents scenarios where the value of a is lower than M ($a > M$). It can be clearly observed that regardless of changes in the parameter value and observation angle, a black region always exists in the image. This is because some photons emitted within the event horizon are captured by it, while others manage to escape towards infinity. The photons that fail to reach the observer create a black region known as the inner shadow. However, the inner shadow region undergoes progressive deformation as the viewing angle increases, transitioning from a disk-like structure ($\theta_o = 0^\circ$) to a hat-like shape ($\theta_o = 83^\circ$). Another notable characteristic is that, regardless of variations in the system's parameters, a distinct bright closed-loop curve consistently encircles the outer boundary of the inner shadow region, marking the position of the critical curve. The significance lies in the fact that irrespective of the spin and deformation parameters of the black hole, the internal shadows and critical curves remain discernible under both low and high angle observations, thereby indicating their intrinsic nature as spacetime features of the black hole.

In Figure 6, i.e., $a < M$, an increase in the deformation parameter ξ will result in an enlargement of the inner shadow region (first and second columns), whereas an increase in the rotation parameter a will lead to a reduction of its size (second and third columns). Therefore, changes in rotation parameter a and deformation parameters ξ show mutually exclusive effects on the size of inner shadow. Additionally, the observed images of the bright bands of light surrounding the black hole at low observation angles, i.e., $\theta_o = 0^\circ$ (first line) and $\theta_o = 17^\circ$ (second line), reveal such a high concentration in brightness distribution that distinguishing between direct and lensed images becomes challenging. To put it more precisely, when the observational inclination is low, the secondary image of the black hole is incorporated into the primary image. When $\theta_o = 83^\circ$ (third line), the direct image and lensed image of black hole are distinguishable. The increase of the

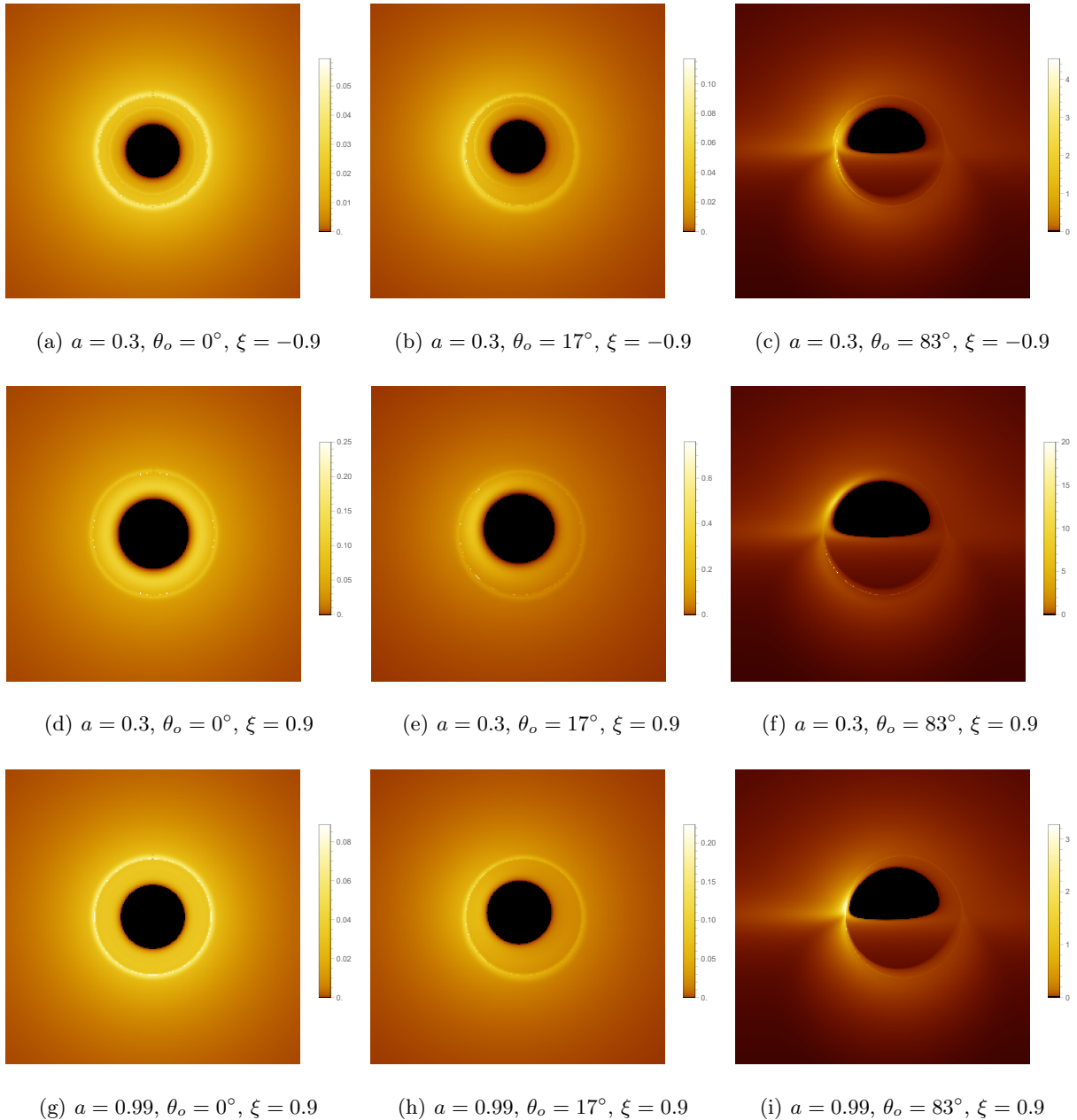


FIG. 6: The image of the Konoplya-Zhidenko rotating non-Kerr black hole surrounded by a prograde thin accretion disk at 230 GHz, where the parameter values are taken as $a < M$. For all images, the mass M is set to $M = 1$, the observer's position is fixed at $r_{obs} = 500M$, and the black hole's event horizon is depicted as a black region.

deformation parameter ξ and rotation parameter a in Figure 7, i.e., when $a > M$, has a similar impact on the size of the inner shadow region as the increase of $a < M$. Moreover, distinguishing between the direct image and lensed image is only possible at higher observation angles.

On the other hand, changes in the parameter space and observation angles will affect the bright-

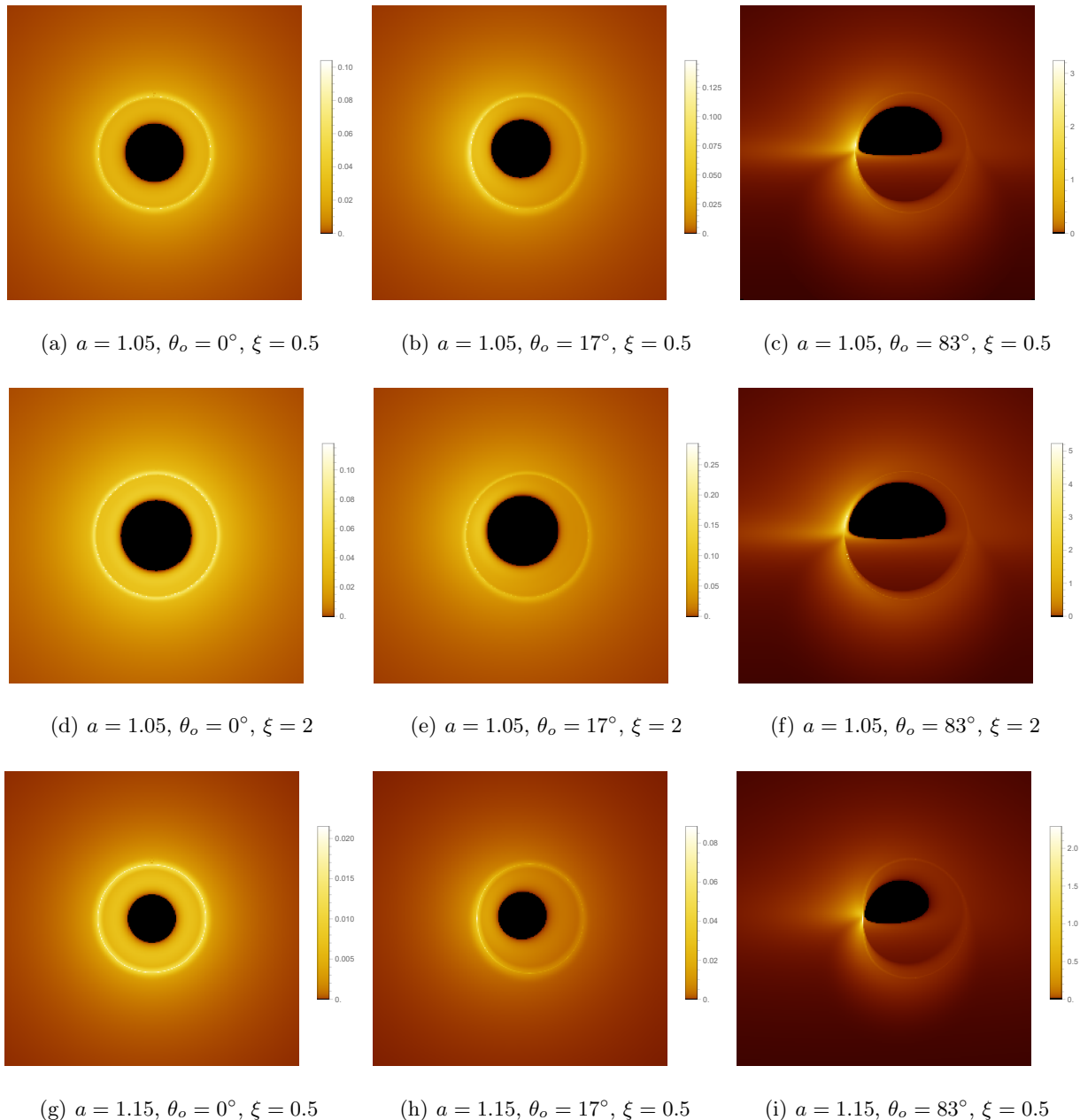


FIG. 7: The image of the Konoplya-Zhidenko rotating non-Kerr black hole surrounded by a prograde thin accretion disk at 230 GHz, where the parameter values are taken as $a > M$. For all images, the mass M is set to $M = 1$, the observer's position is fixed at $r_{obs} = 500M$, and the black hole's event horizon is depicted as a black region.

ness of the image. The result show that the central brightness depression is a characteristic phenomenon observed in all cases where the accretion disk is not excessively thick. When the angle of observation is $\theta_o = 0^\circ$, the brightness of the image exhibits symmetry in both horizontal and vertical directions. However, as the angle of observation increases, the asymmetry of image bright-

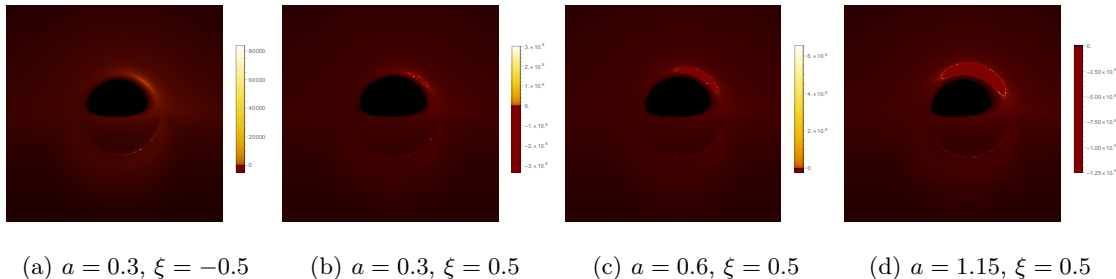


FIG. 8: The image of the Konoplya-Zhidenko rotating non-Kerr black hole surrounded by a retrograde thin accretion disk at 230 GHz, where the observed inclination is taken as $\theta_o = 83^\circ$. For all images, the mass M is set to $M = 1$, the observer's position is fixed at $r_{obs} = 500M$, and the black hole's event horizon is depicted as a black region.

ness in the horizontal direction gradually intensifies. In particular, when the angle of observation is $\theta_o = 83^\circ$, there is a noticeable disparity in radiation flux intensity between the left and right sides of the image. This phenomenon arises from the Doppler effects occurring on the left side of the screen, which are attributed to the prograde accretion disk's forward rotation.

Now, we will elucidate the geometric intricacies of the retrograde accretion disk observed on the observer's screen. Figure 8 illustrates the impact of variations in spin parameters a and deformation parameters ξ on the image of a Konoplya-Zhidenko rotating non-Kerr black hole, which is surrounded by an accretion disk with retrograde flows. The first three columns correspond to the scenario where the spin parameter a is less than the mass M ($a < M$), while the fourth column pertains to the situation where the spin parameter a exceeds the mass M ($a > M$). Based on Figure 8, the inner shadow region consistently appears in the image across various parameter spaces. It is evident that, irrespective of the orientation of the accretion disk, an increase in the observed inclination angle enables a clear differentiation between direct and lensing images, and that the change in parameter space has the same effect on the inner shadow region as it does on the prograde case. In comparison to the prograde scenario, the observed representation of the black hole image is markedly diminished due to gravitational redshift. At the same observation frequency, the optical depth diminished the visibility of the lensed image, displaying solely the upper half of the image on the screen. This phenomenon can be attributed to the fact that, in the simulation of black hole images, the luminous material contributing to the increased total optical depth is primarily located within the equatorial plane, whereas the jet material situated in front of the event horizon exhibits lower brightness. Thus, although the direct geometric effect of equatorial radiation being truncated at the event horizon is almost invisible, it can still be observed. On the other hand, a

crested or eyebrow-shaped bright region appears in the upper right quadrant of the display, and an increase in parameters a and ξ will correspondingly expand the extent of this region.

V. DISTRIBUTION OF THE REDSHIFT FACTORS

The examination of how light from the accretion disk surrounding the black hole reaches the observer's plane necessitates careful consideration of variations in light intensity, which are influenced by a combination of divergence, absorption, Doppler effect, and gravitational redshift. The relative motion between the accretion disk and distant observers offers us a unique perspective into the intricate interactions between black holes and accretion disks, as well as the nature of their formation. The Doppler effect plays a significant role in explaining such phenomena, while the gravitational redshift, as a crucial indicator for revealing the impact of an extreme gravitational field, cannot be disregarded. Therefore, in the process of imaging a black hole, it is crucial to accurately assess the redshift factor associated with the behavior of emitted particles, as this step plays a critical role in precisely characterizing both the black hole and its accretion disk.

In Figures 9 and 10, we present the redshift factors of the direct and lensed images of the anteroonal accretion disk for the case where $a < M$, while the other parameter values correspond to those in Figure 6. A continuous linear color map is utilized to visually represent the redshift factor, with red indicating redshift and blue indicating blueshift. The central black region of each observing plane represents the inner shadow cast by the accretion disk, which is bounded by the projection of the event horizon of the black hole. It can be observed that when the observed inclination value is small, such as $\theta_o = 0^\circ$ and $\theta_o = 17^\circ$, the observer's screen mainly displays a redshift feature. When the observation inclination is a large value, such as $\theta_o = 83^\circ$, in addition to the redshift on the observer screen will also appear obvious blue shift phenomenon, and mainly distributed on the left side of the screen, while the redshift is mainly distributed on the right side. Furthermore, the modification of pertinent parameters exerts a substantial influence on the redshift and blueshift phenomena observed in black hole imagery. Specifically, an increment in the deformation parameter ξ results in a reduction of the redshift range while simultaneously expanding the blue shift range. Conversely, an augmentation of the rotational parameter a leads to a substantial diminution in both the redshift and blue shift ranges. For the lensed image depicted in Figure 10, a redshift is observed exclusively at low obliquity angles ($\theta_o = 0^\circ$ and $\theta_o = 17^\circ$), which aligns with the characteristics of the direct image. When the observed inclination is $\theta_o = 83^\circ$, a minor petal-shaped blueshift appears on the lower right side of the screen, while the redshift remains in proximity to the ISCO.

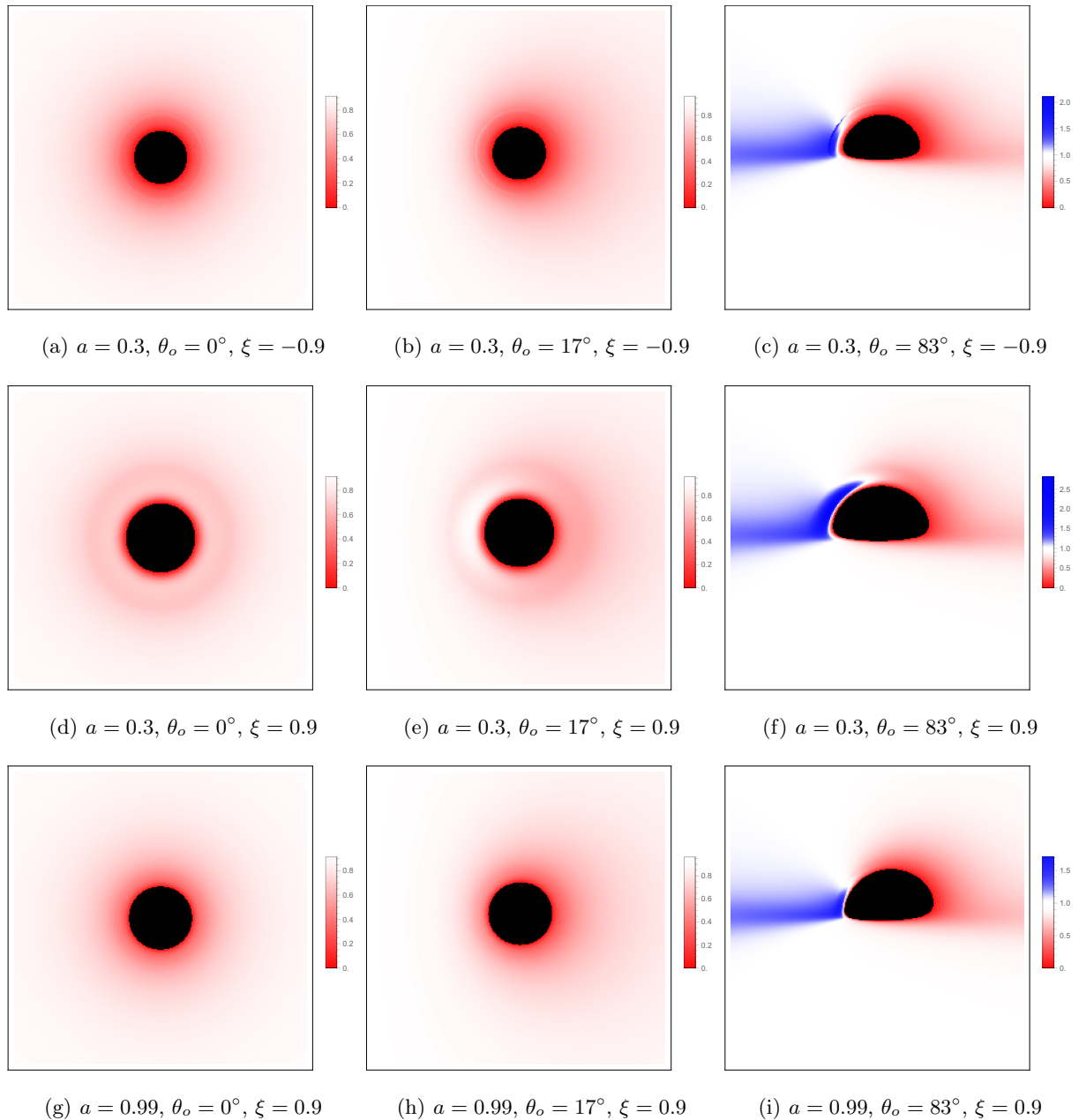


FIG. 9: The redshift distribution of direct images under prograde disk, where the parameter values are taken as $a < M$. The red and blue hues denote the redshift and blueshift, respectively, while the shaded black region represents the event horizon of the black hole. In addition, set the mass of the black hole to $M = 1$ and fix the observer's position at $r_{obs} = 500M$.

Furthermore, an increase in the deformation parameter ξ linearly enlarges the shadow's size while notably diminishing the redshift and blueshift observed at the edge of the black disk. Similarly, decreasing the value of parameter a produces analogous effects.

For the case of $a > M$, the redshift factors of the direct and lensed images of the prograde

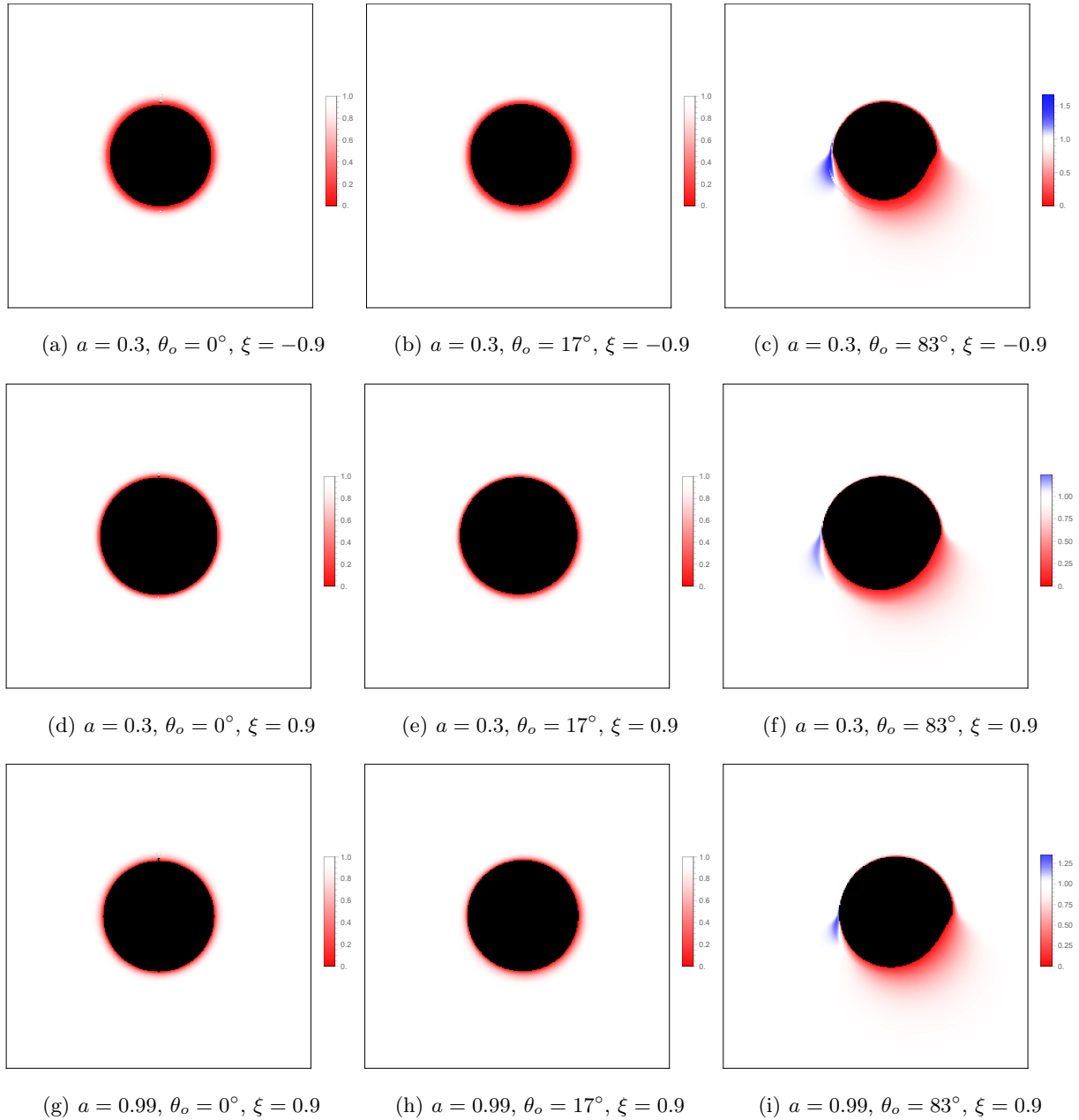


FIG. 10: The redshift distribution of lensed images under prograde disk, where the parameter values are taken as $a < M$. The red and blue hues denote the redshift and blueshift, respectively, while the shaded black region represents the event horizon of the black hole. In addition, set the mass of the black hole to $M = 1$ and fix the observer's position at $r_{obs} = 500M$.

accretion disk are presented in Figures 11 and 12, respectively. It is observed that as the observation angle increases from 0 to $\pi/2$, the region of blueshift gradually expands, especially near the ISCO, where a more pronounced blueshift is evident. Simultaneously, an increase in the deformation parameter ξ or a decrease in the rotation parameter a will result in an expansion of the inner shadow

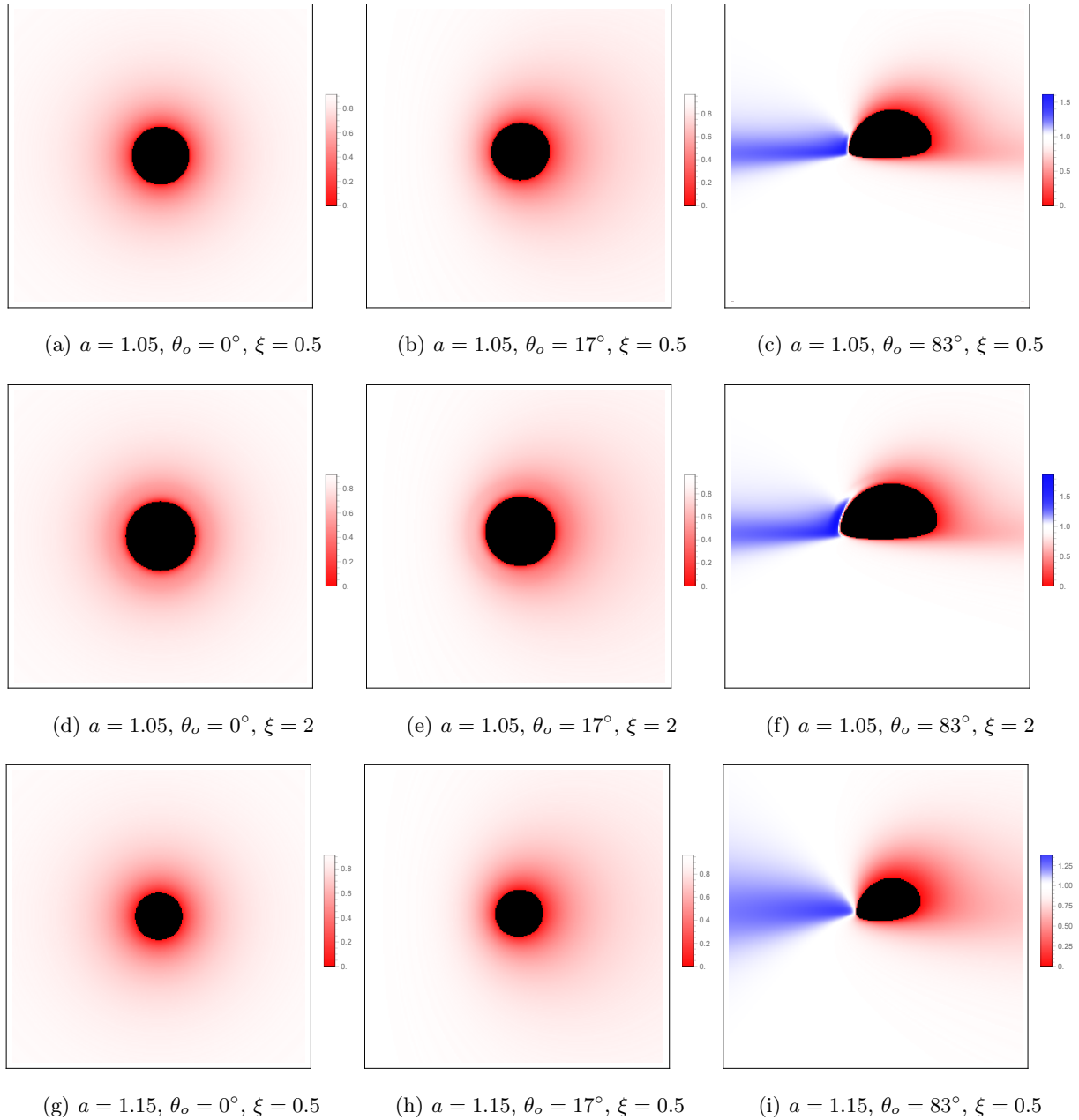


FIG. 11: The redshift distribution of direct images under prograde disk, where the parameter values are taken as $a > M$. The red and blue hues denote the redshift and blueshift, respectively, while the shaded black region represents the event horizon of the black hole. In addition, set the mass of the black hole to $M = 1$ and fix the observer's position at $r_{obs} = 500M$.

region, concurrently leading to a gradual reduction in redshift and a progressive enhancement of blueshift.

The images presented in Figures 13 depict the outcomes achieved when the direction of the accretion flow is retrograde. Figures 13 primarily illustrates the distribution of the redshift factor

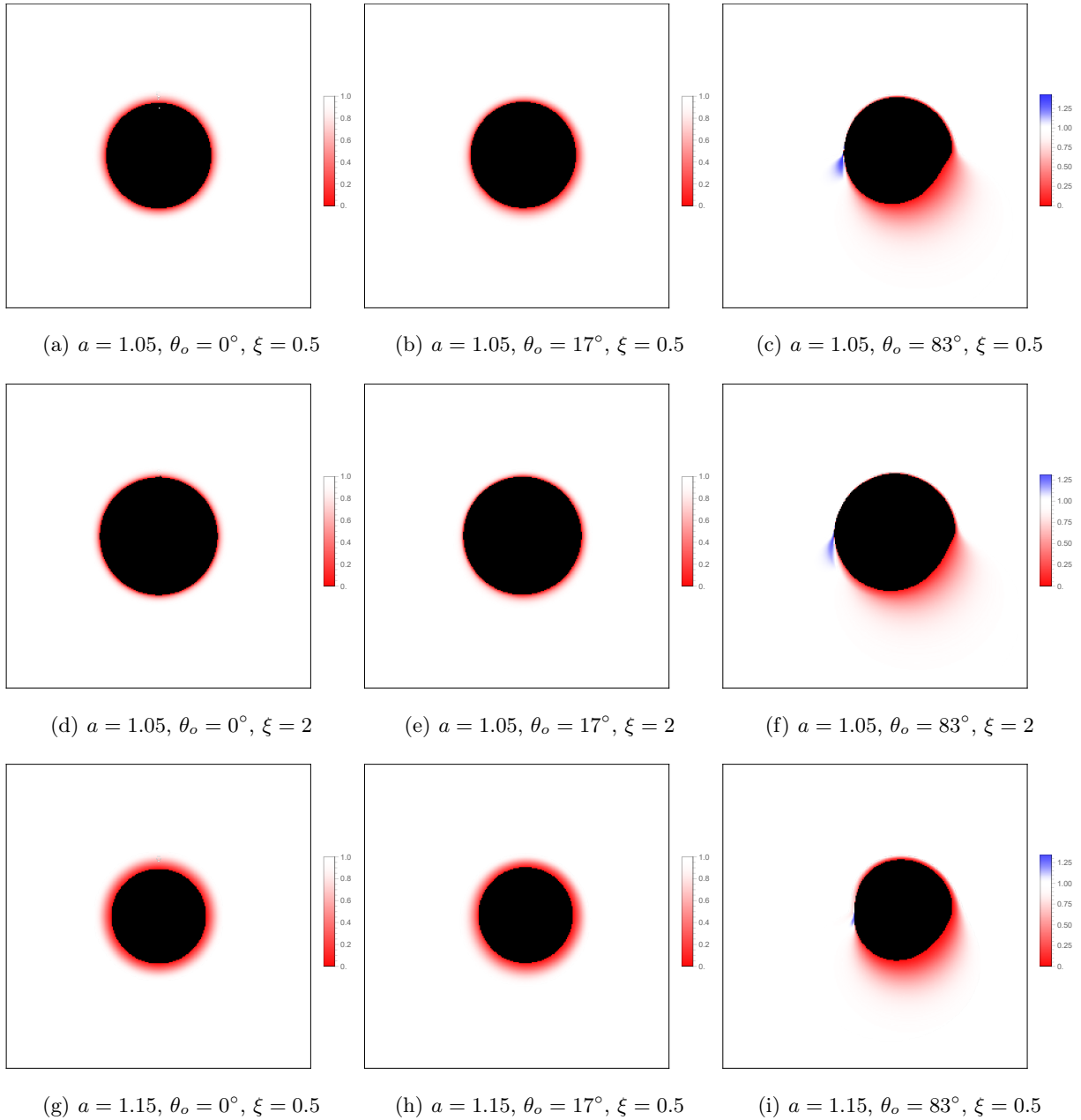


FIG. 12: The redshift distribution of lensed images under prograde disk, where the parameter values are taken as $a > M$. The red and blue hues denote the redshift and blueshift, respectively, while the shaded black region represents the event horizon of the black hole. In addition, set the mass of the black hole to $M = 1$ and fix the observer's position at $r_{obs} = 500M$.

for the direct image (first line) and lensed image (second line) at $\theta_o = 80^\circ$. For the direct images, it is evident that as parameters A and B increase, the redshift lensing effect manifests within the blueshift region. This phenomenon is attributed to retrograde accretion flows and relativistic jets, which are predominantly situated along the equatorial plane, where most of the emission originates.

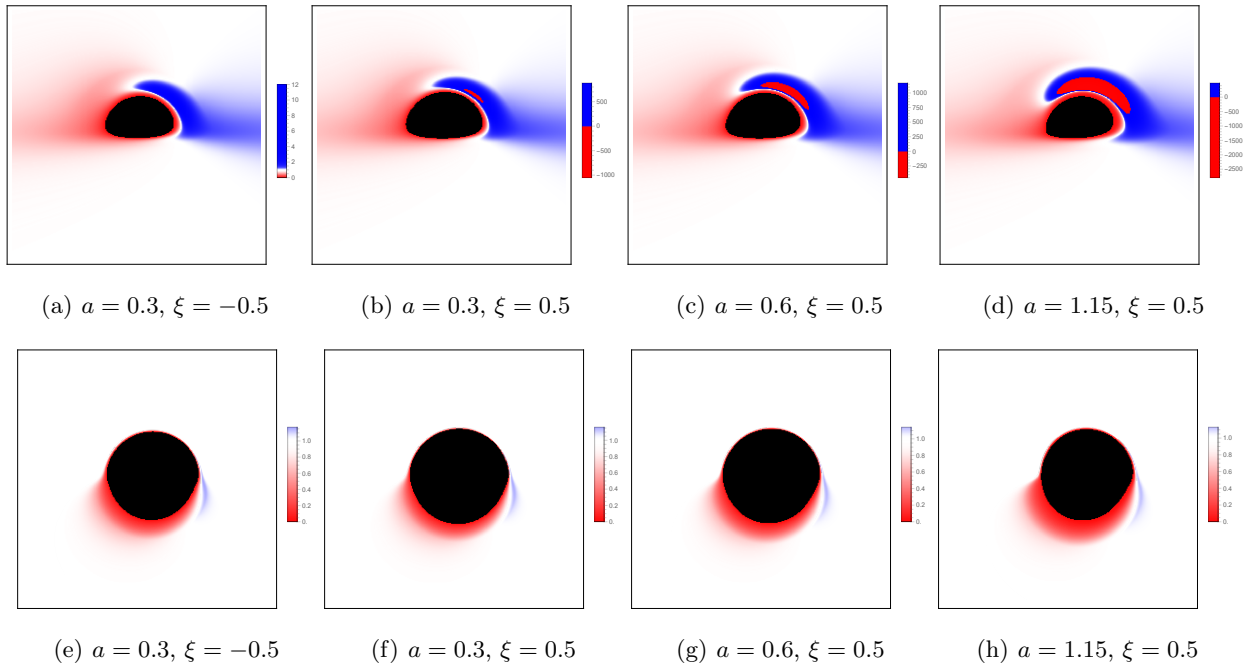


FIG. 13: The image of a Konoplya-Zhidenko rotational non-Kerr black hole surrounded by a prograde thin accretion disk at observation angle $\theta_o = 83^\circ$.

For lensed images, only the lower right quadrant of the screen exhibits a minor blue shift, and its contour manifests as an irregular arc. The radiation from the accretion disk is inversely directed, leading to a central luminance depression that is marginally smaller than the equatorial inner shadow region. This occurs because the radiation emanates from regions that intersect the event horizon at their maximum latitude within the equatorial plane.

VI. CONCLUSIONS AND DISCUSSIONS

Significant advancements in the detection of GWs and the imaging of black holes signify that we are entering an unprecedented era for testing the physics of strong gravitational fields. The formation of a black hole shadow is fundamentally due to the deflection of light in an intense gravitational field, and its image can provide crucial insights into the geometry of spacetime. Research on black hole shadows across different types of black holes is a rapidly developing field that not only elucidates black hole properties but also offers potential tests for modified gravity theories. The Konoplya-Zhidenko rotational non-Kerr spacetime has some non-negligible deviations from the Kerr spacetime, and the quasi-periodic oscillations and the constraints of iron lines also support that a real astrophysical black hole can be described by the Konoplya-Zhidenko rotational non-Kerr

metric. In this paper, we investigate the shadow and optical observed properties of a Konoplya-Zhidenko rotating non-Kerr metric black hole to explore the observed differences between different parameters. As an initial step, we investigate the dynamics of photons in the vicinity of Konoplya-Zhidenko rotational non-Kerr black hole and constrain the relevant parameters of this spacetime based on astronomical observations of M87* and Sgr A*. To acquire the observational image of the black hole from the perspective of a ZAMO, we propose positioning an optically and geometrically thin accretion disk on the equatorial plane of the black hole, serving as the sole background light source. We extend the classical accretion disk model to a scenario in which the innermost region of the accretion disk extends to the event horizon of the black hole. Furthermore, the accretion materials consist of electrically neutral plasma, and their motion within the accretion disk is categorized into two types based on the ISCO. Specifically, the ISCO delineates the boundary beyond which the emission spectrum from accretion disks will exhibit stable circular orbits. Within this boundary, however, material is subject to critical plunging orbits. Using fisheye camera ray-tracing techniques, we conducted a detailed analysis of the image of a thin accretion disk surrounding a Konoplya-Zhidenko rotating non-Kerr black hole, where the motion of the accretion disk in two ways, i.e., prograde and retrograd.

Firstly, we investigate the image of a Konoplya-Zhidenko rotating non-Kerr metric black hole encompassed by a prograde thin accretion disk. In all these images, one can consistently observe a prominent dark region surrounded by a narrow photon ring. The dark region corresponds to the accretion disk profile at $r = r_h$, commonly referred to as the inner shadow, while the photon ring aligns closely with the critical curve of the black hole. Regardless of whether $a > M$ or $a < M$, an increase in the rotation parameter reduces the area of the inner shadow region, whereas an increase in the deformation parameter produces the opposite effect. At low observation angles, that is, $\theta_o = 0^\circ$ and $\theta_o = 17^\circ$, although the shadow region in $\theta_o = 17^\circ$ has a slight deformation and moves to the upper left of the image screen, it does not show obvious photon ring concentric circles like $\theta_o = 0^\circ$, but the difference in brightness distribution near the image is not obvious, so that the direct image and the lens image cannot be directly distinguished. When the observed inclination is $\theta_o = 80^\circ$, the deformation of the inner shadow region becomes clearly identifiable, exhibiting a shape reminiscent of a hat. Then, a clear distinction can be made between the direct image and the lensed image. Notably, a prominent feature emerges on the left side of the screen: a bright crescent or eyebrow-shaped area that contributes to the amplification of the angle, thereby enhancing the Doppler effect. To accurately analyze the true situation of accreting material around the black hole, we conducted an in-depth investigation into the redshift factor of both the direct

and lensed images. In the case of direct images, the results indicate that at an smaller observation angle ($\theta_o = 0^\circ$ and $\theta_o = 17^\circ$), the observer can only detect the redshift factor on the screen. As θ_o increase to $\theta_o = 83^\circ$, a blueshift is also observed on the left side of the screen. In the case of the lensed image, the observed inclination changes are analogous to those observed in the direct image. However, a notable distinction is the petal-like blue shift that appears on the left side of the screen when $\theta_o = 83^\circ$, which is considerably smaller in magnitude compared to the direct image results. Furthermore, the alteration of the parameter space will result in modifications to the ranges of redshift and blueshift, but these changes are unlikely to significantly affect the overall characteristics.

Subsequently, we examine the image of a Konoplya-Zhidenko rotating non-Kerr black hole, wherein the accretion disk exhibits retrograde motion. It is evident that irrespective of the orientation of the accretion disk, the black hole's intrinsic shadow remains invariant under identical parameters. Likewise, when the angle of observation is sufficiently large, it becomes feasible to differentiate between the direct image and the lensed image. Undoubtedly, there are distinct differences in the imagery of prograde and retrograde accretion disks. As the parameters (a, ξ) increase, a bright region resembling a crescent moon or eyebrow emerges in the upper right quadrant of the screen, which is not observed in the prograde scenario. This phenomenon arises due to the gravitational redshift of the accretion disk being merged in the case of retrograde flows. In addition, the redshift and blue shift areas are interchanged on the screen compared with the prograde flows case. Our current analysis indicates that the aforementioned discussion could yield significant insights for the theoretical investigation of black hole shadows and their associated dynamics. We anticipate that this work will contribute to the theoretical research of high-resolution accretion disk imaging in the future, and offer valuable inspiration for validating general relativity and other modified gravitational theories.

Acknowledgements

This work is supported by the National Natural Science Foundation of China (Grant Nos. 11875095 and 11903025) and by the Natural Science Foundation of Chongqing (CSTB2023NSCQ-MSX0594).

[1] B. P. Abbott *et al.* [LIGO Scientific and Virgo], Phys. Rev. Lett. **116**, no.24, 241103 (2016)

- [2] B. P. Abbott *et al.* [LIGO Scientific and Virgo], Phys. Rev. Lett. **116**, no.24, 241102 (2016)
- [3] B. P. Abbott *et al.* [LIGO Scientific and Virgo], Phys. Rev. Lett. **116**, no.6, 061102 (2016)
- [4] K. Akiyama *et al.* [Event Horizon Telescope], Astrophys. J. Lett. **875**, L1 (2019)
- [5] K. Akiyama *et al.* [Event Horizon Telescope], Astrophys. J. Lett. **875**, no.1, L2 (2019)
- [6] K. Akiyama *et al.* [Event Horizon Telescope], Astrophys. J. Lett. **875**, no.1, L3 (2019)
- [7] K. Akiyama *et al.* [Event Horizon Telescope], Astrophys. J. Lett. **875**, no.1, L4 (2019)
- [8] K. Akiyama *et al.* [Event Horizon Telescope], Astrophys. J. Lett. **875**, no.1, L5 (2019)
- [9] K. Akiyama *et al.* [Event Horizon Telescope], Astrophys. J. Lett. **875**, no.1, L6 (2019)
- [10] K. Akiyama *et al.* [Event Horizon Telescope], Astrophys. J. Lett. **930**, no.2, L12 (2022)
- [11] K. Akiyama *et al.* [Event Horizon Telescope], Astrophys. J. Lett. **930**, no.2, L13 (2022)
- [12] K. Akiyama *et al.* [Event Horizon Telescope], Astrophys. J. Lett. **930**, no.2, L14 (2022)
- [13] K. Akiyama *et al.* [Event Horizon Telescope], Astrophys. J. Lett. **930**, no.2, L15 (2022)
- [14] K. Akiyama *et al.* [Event Horizon Telescope], Astrophys. J. Lett. **930**, no.2, L16 (2022)
- [15] K. Akiyama *et al.* [Event Horizon Telescope], Astrophys. J. Lett. **930**, no.2, L17 (2022)
- [16] P. V. P. Cunha and C. A. R. Herdeiro, Gen. Rel. Grav. **50**, no.4, 42 (2018)
- [17] J. L. Synge, Mon. Not. Roy. Astron. Soc. **131**, no.3, 463-466 (1966)
- [18] J.M. Bardeen, Proceedings, Ecole d'Eté de Physique Théorique: Les Astres Occlus: Les Houches, France, August, 1972, pp. 215-240 (1973)
- [19] S. Chandrasekhar, The Mathematical Theory of Black Holes, Oxford University Press, New York (1992)
- [20] K. Hioki and K. i. Maeda, Phys. Rev. D **80**, 024042 (2009)
- [21] Y. Kumaran and A. Övgün, Eur. Phys. J. C **83**, no.9, 812 (2023)
- [22] P. H. Mou, Y. X. Chen, K. J. He and G. P. Li, Commun. Theor. Phys. **74**, no.12, 125401 (2022)
- [23] K. J. He, Y. W. Han and G. P. Li, Nucl. Phys. B **1010**, 116768 (2025)
- [24] K. J. He, Y. W. Han and G. P. Li, Phys. Dark Univ. **44**, 101468 (2024)
- [25] K. J. He, Z. Luo, S. Guo and G. P. Li, Chin. Phys. C **48**, no.6, 065105 (2024)
- [26] A. Abdujabbarov, M. Amir, B. Ahmedov and S. G. Ghosh, Phys. Rev. D **93**, no.10, 104004 (2016)
- [27] X. X. Zeng, G. P. Li and K. J. He, Nucl. Phys. B **974**, 115639 (2022)
- [28] S. W. Wei, P. Cheng, Y. Zhong and X. N. Zhou, JCAP **08**, 004 (2015)
- [29] F. Atamurotov and B. Ahmedov, Phys. Rev. D **92**, 084005 (2015)
- [30] V. Perlick, O. Y. Tsupko and G. S. Bisnovatyi-Kogan, Phys. Rev. D **92**, no.10, 104031 (2015)
- [31] F. Atamurotov, K. Jusufi, M. Jamil, A. Abdujabbarov and M. Azreg-Aïnou, Phys. Rev. D **104**, no.6, 064053 (2021)
- [32] V. Perlick and O. Y. Tsupko, Phys. Rept. **947**, 1-39 (2022)
- [33] M. Wang, S. Chen and J. Jing, Commun. Theor. Phys. **74**, no.9, 097401 (2022)
- [34] S. Chen, J. Jing, W. L. Qian and B. Wang, Sci. China Phys. Mech. Astron. **66**, no.6, 260401 (2023)
- [35] K. J. He, J. T. Yao, X. Zhang and X. Li, Phys. Rev. D **109**, no.6, 064049 (2024)

- [36] M. Guo and P. C. Li, *Eur. Phys. J. C* **80**, no.6, 588 (2020)
- [37] F. Atamurotov, A. Abdujabbarov and B. Ahmedov, *Phys. Rev. D* **88**, no.6, 064004 (2013)
- [38] R. A. Konoplya, *Phys. Lett. B* **795**, 1-6 (2019)
- [39] R. Shaikh, P. Kocherlakota, R. Narayan and P. S. Joshi, *Mon. Not. Roy. Astron. Soc.* **482**, no.1, 52-64 (2019)
- [40] L. Amarilla and E. F. Eiroa, *Phys. Rev. D* **85**, 064019 (2012)
- [41] U. Papnoi, F. Atamurotov, S. G. Ghosh and B. Ahmedov, *Phys. Rev. D* **90**, no.2, 024073 (2014)
- [42] Y. Meng, X. M. Kuang, X. J. Wang and J. P. Wu, *Phys. Lett. B* **841**, 137940 (2023)
- [43] Z. Zhang, Y. Hou and M. Guo, *Chin. Phys. C* **48**, no.8, 085106 (2024)
- [44] X. X. Zeng, L. F. Li, P. Li, B. Liang and P. Xu, *Sci. China Phys. Mech. Astron.* **68**, no.2, 220412 (2025)
- [45] X. X. Zeng, K. J. He, J. Pu, G. p. Li and Q. Q. Jiang, *Eur. Phys. J. C* **83**, no.10, 897 (2023)
- [46] Y. Liu, Q. Chen, X. X. Zeng, H. Zhang, W. L. Zhang and W. Zhang, *JHEP* **10**, 189 (2022)
- [47] Z. Younsi, A. Zhidenko, L. Rezzolla, R. Konoplya and Y. Mizuno, *Phys. Rev. D* **94**, no.8, 084025 (2016)
- [48] R. A. Konoplya and A. Zhidenko, *Phys. Rev. D* **103**, no.10, 104033 (2021)
- [49] A. R. Soares, C. F. S. Pereira, R. L. L. Vitória and E. M. Rocha, *Phys. Rev. D* **108**, no.12, 124024 (2023)
- [50] A. R. Soares, R. L. L. Vitória and C. F. S. Pereira, *Phys. Rev. D* **110**, no.8, 084004 (2024)
- [51] N. Tsukamoto, Z. Li and C. Bambi, *JCAP* **06**, 043 (2014)
- [52] R. A. Konoplya, *Phys. Lett. B* **804**, 135363 (2020)
- [53] Z. Zhong, Z. Hu, H. Yan, M. Guo and B. Chen, *Phys. Rev. D* **104**, no.10, 104028 (2021)
- [54] J. Huang, Z. Zhang, M. Guo and B. Chen, *Phys. Rev. D* **109**, no.12, 124062 (2024)
- [55] X. Wang, X. Wang, H. Q. Zhang and M. Guo, *Eur. Phys. J. C* **84**, no.11, 1168 (2024)
- [56] J. P. Luminet, *Astron. Astrophys.* **75**, 228-235 (1979)
- [57] R. Narayan, M. D. Johnson and C. F. Gammie, *Astrophys. J. Lett.* **885**, no.2, L33 (2019)
- [58] X. X. Zeng, H. Q. Zhang and H. Zhang, *Eur. Phys. J. C* **80**, no.9, 872 (2020)
- [59] M. Heydari-Fard, M. Heydari-Fard and N. Riazi, *Int. J. Mod. Phys. D* **32**, no.13, 2350088 (2023)
- [60] S. E. Gralla, D. E. Holz and R. M. Wald, *Phys. Rev. D* **100**, no. 2, 024018 (2019)
- [61] X. X. Zeng and H. Q. Zhang, *Eur. Phys. J. C* **80**, no.11, 1058 (2020)
- [62] J. Peng, M. Guo and X. H. Feng, *Chin. Phys. C* **45**, no.8, 085103 (2021)
- [63] K. J. He, S. C. Tan and G. P. Li, *Eur. Phys. J. C* **82**, no.1, 81 (2022)
- [64] G. P. Li and K. J. He, *Eur. Phys. J. C* **81**, no.11, 1018 (2021)
- [65] X. X. Zeng, K. J. He and G. P. Li, *Sci. China Phys. Mech. Astron.* **65**, no.9, 290411 (2022)
- [66] S. Guo, K. J. He, G. R. Li and G. P. Li, *Class. Quant. Grav.* **38**, no.16, 165013 (2021)
- [67] G. P. Li and K. J. He, *JCAP* **06**, 037 (2021)
- [68] X. J. Gao, T. T. Sui, X. X. Zeng, Y. S. An and Y. P. Hu, *Eur. Phys. J. C* **83**, 1052 (2023)

- [69] Y. H. Cui, S. Guo, Y. X. Huang, Y. Liang and K. Lin, *Eur. Phys. J. C* **84**, no.8, 772 (2024)
- [70] K. J. He, S. Guo, S. C. Tan and G. P. Li, *Chin. Phys. C* **46**, no.8, 085106 (2022)
- [71] H. M. Wang, Z. C. Lin and S. W. Wei, *Nucl. Phys. B* **985**, 116026 (2022)
- [72] Y. Hou, Z. Zhang, H. Yan, M. Guo and B. Chen, *Phys. Rev. D* **106**, no.6, 064058 (2022)
- [73] C. Y. Yang, M. I. Aslam, X. X. Zeng and R. Saleem, [arXiv:2411.11807 [astro-ph.HE]]
- [74] S. Guo, Y. X. Huang, E. W. Liang, Y. Liang, Q. Q. Jiang and K. Lin, *Astrophys. J.* **975**, no.2, 237 (2024)
- [75] K. J. He, G. P. Li, C. Y. Yang and X. X. Zeng, [arXiv:2411.11680 [astro-ph.HE]]
- [76] G. P. Li, H. B. Zheng, K. J. He and Q. Q. Jiang, [arXiv:2410.17295 [gr-qc]]
- [77] T. Johannsen and D. Psaltis, *Phys. Rev. D* **83**, 124015 (2011)
- [78] R. Konoplya and A. Zhidenko, *Phys. Lett. B* **756**, 350-353 (2016)
- [79] R. Konoplya, L. Rezzolla and A. Zhidenko, *Phys. Rev. D* **93**, no.6, 064015 (2016)
- [80] C. Bambi, *JCAP* **09**, 014 (2012)
- [81] C. Bambi, *Eur. Phys. J. C* **75**, no.4, 162 (2015)
- [82] L. Kong, Z. Li and C. Bambi, *Astrophys. J.* **797**, no.2, 78 (2014)
- [83] C. Bambi, *Phys. Lett. B* **705**, 5-8 (2011)
- [84] T. Johannsen and D. Psaltis, *Astrophys. J.* **773**, 57 (2013)
- [85] J. Jiang, C. Bambi and J. F. Steiner, *JCAP* **05**, 025 (2015)
- [86] C. Bambi, *JCAP* **08**, 055 (2013)
- [87] S. Wang, S. Chen and J. Jing, *JCAP* **11**, 020 (2016)
- [88] F. Long, S. Chen, S. Wang and J. Jing, *Nucl. Phys. B* **926**, 83-94 (2018)
- [89] P. V. P. Cunha, C. A. R. Herdeiro and E. Radu, *Phys. Rev. D* **96**, no.2, 024039 (2017)
- [90] F. Long, S. Wang, S. Chen and J. Jing, [arXiv:2409.11942 [gr-qc]]
- [91] G. He, G. Huang and A. Hu, *Symmetry* **15**, no.10, 1848 (2023)
- [92] S. Patra, B. R. Majhi and S. Das, *JHEAp* **44**, 371-380 (2024)
- [93] M. Wang, S. Chen and J. Jing, *JCAP* **10**, 051 (2017)
- [94] K. Hioki and K. i. Maeda, *Phys. Rev. D* **80**, no.2, 024042 (2009)
- [95] L. Amarilla and E. F. Eiroa, *Phys. Rev. D* **85**, no.6, 064019 (2012)
- [96] W. T. Liu, D. Wu, X. J. Fang, J. Jing and J. C. Wang, arXiv:2406.00579 [gr-qc] (2024)
- [97] W. T. Liu, D. Wu and J. C. Wang, *Phys. Lett. B* **858**, 139052 (2024)
- [98] S. Capozziello, S. Zare and H. Hassanabadi, arXiv:2311.12896 [gr-qc] (2023)
- [99] R. K. Walia, S. G. Ghosh and S. D. Maharaj, *Astrophys. J.* **939**, no.2, 77 (2022)
- [100] M. Wang, G. Guo, P. Yan, S. Chen and J. Jing, *Chin. Phys. C* **48**, no.10, 105103 (2024)
- [101] B. P. Abbott *et al.* [LIGO Scientific and Virgo], *Phys. Rev. Lett.* **116**, no.22, 221101 (2016)
- [102] Z. Hu, Z. Zhong, P. C. Li, M. Guo and B. Chen, *Phys. Rev. D* **103**, no.4, 044057 (2021)
- [103] A. Chael, M. D. Johnson and A. Lupsasca, *Astrophys. J.* **918**, no.1, 6 (2021)
- [104] K. Wang, C. J. Feng and T. Wang, *Eur. Phys. J. C* **84**, no.5, 457 (2024)